LAWRENCE
LIVERMORE
NATIONAL
LABORATORY

LLNL-JRNL-413781

Phase Separation of Lipid Membranes Analyzed with High-Resolution Secondary-Ion Mass Spectrometry

M. L. Kraft, P. K. Weber, M. L. Longo, I. D. Hutcheon, S. G. Boxer

June 10, 2009

Science

Disclaimer

This document was prepared as an account of work sponsored by an agency of the United States government. Neither the United States government nor Lawrence Livermore National Security, LLC, nor any of their employees makes any warranty, expressed or implied, or assumes any legal liability or responsibility for the accuracy, completeness, or usefulness of any information, apparatus, product, or process disclosed, or represents that its use would not infringe privately owned rights. Reference herein to any specific commercial product, process, or service by trade name, trademark, manufacturer, or otherwise does not necessarily constitute or imply its endorsement, recommendation, or favoring by the United States government or Lawrence Livermore National Security, LLC. The views and opinions of authors expressed herein do not necessarily state or reflect those of the United States government or Lawrence Livermore National Security, LLC, and shall not be used for advertising or product endorsement purposes.

Phase Separation of Lipid Membranes Analyzed with High-Resolution Secondary-Ion Mass Spectrometry

Mary L. Kraft[*], Peter K. Weber[†], Marjorie L. Longo[‡], Ian D. Hutcheon[†], Steven G. Boxer[*]

[*]Department of Chemistry, Stanford University, Stanford, CA 94305
[†] Glenn T. Seaborg Institute & BioSecurity and Nanosciences Laboratory, Lawrence Livermore National Laboratory, Livermore, CA 94551
[‡]Department of Chemical Engineering and Material Science, University of California, Davis, CA 95616

Abstract

Lateral variations in membrane composition are postulated to play a central role in many cellular events, but it has been difficult to probe membrane composition and organization on the tens to hundreds of nanometer length scale that bridges atomic resolution structures of membrane components and imaging with light microscopy. We present a high-resolution imaging secondary-ion mass spectrometry (NanoSIMS) technique to reveal the lipid distribution within a phase-separated membrane with a lateral resolution of ~100 nanometers. Quantitative information was obtained on the chemical composition within small lipid domains using isotopic labels to identify each molecular species. Composition variations were detected within some domains.

Imaging and quantifying the static and dynamic variations in lateral composition that result from interactions among membrane components is a major challenge in structural biology. Although biological membranes are fluid structures and fluidity is essential for function, it is widely believed that some degree of lateral organization is present and that this organization is also essential for function *(1-3)(1-3)*. The relevant distance scale is larger than that of individual membrane proteins or protein assemblies (> 10 nm), whose structures can be determined by x-ray crystallography or inferred from atomic force microscopy (AFM), but substantially below the diffraction limit of light microscopy. Fluorescence microscopy is widely used and is extremely sensitive and specific to the labeled component *(4-8)*(*4-8*), but only the labeled component is observed, and, at least for relatively small components like lipids, the fluorophore may greatly alter the delicate interactions that are present in the membrane *(9)*(*9*). Infrared *(10)*(*10*) and coherent anti-Stokes Raman *(11)*(*11*) imaging offer greater chemical specificity, but thus far the lateral resolution and sensitivity are limited. AFM provides much better resolution of topographical features, but does not yield information on chemical composition *(9, 12-14)*(*9, 12-14*). Imaging mass spectrometry offers distinct advantages over these methods *(15-21)*(*15-21*), and we now apply this approach to imaging and analyzing the chemical composition of small lipid domains with ~ 100 nm lateral resolution.

Secondary-ion mass spectrometry (SIMS) was performed with a NanoSIMS 50 (Cameca Instruments, Courbevoie, France). During NanoSIMS analysis, a focused $^{133}Cs^+$ primary ion beam is rastered across the sample; secondary ions generated by sputtering are extracted and analyzed according to their respective charge-to-mass ratios at high mass resolving power (Fig. 1). By selectively incorporating a distinctive stable isotope into each membrane component, e.g., ^{13}C and ^{15}N, NanoSIMS secondary ion images characteristic of each species, e.g., $^{13}C^{1}H^{-}$ and $^{12}C^{15}N^{-}$, respectively, can be used to create a component-specific compositional map of the sample. Using this approach, we demonstrate the ability to image and analyze quantitatively the composition of very small lipid domains within a phase-separated lipid membrane.

Supported lipid bilayers were prepared from vesicles containing equal mole (mol) fractions of ^{15}N-labeled 1,2-dilauroylphosphatidylcholine [^{15}N-DLPC, melting temperature (T_m) = -5 °C] and ^{13}C-labeled 1,2-distearoylphosphatidylcholine ($^{13}C_{18}$-DSPC, T_m = 55 °C), with 0.5 mol% of a fluorescent lipid added to allow the bilayer quality to be evaluated by fluorescence microscopy during sample preparation (*22*). The sample was maintained at 70 °C, above the T_m of both lipid components to ensure complete mixing, both during vesicle and supported bilayer formation on pre-warmed (70 °C) silicon wafers. The silicon wafers were prepared with a thin (17 nm) SiO_2 layer that facilitated the formation of stable bilayers while permitting charge dissipation during the SIMS analysis, and the wafers were patterned with chrome grids to corral the lipid bilayers and provide landmarks on the surface for characterization of the same regions by fluorescence, AFM, and NanoSIMS imaging (*22, 23*). The homogeneous, supported bilayer samples were slowly cooled to room temperature to induce phase separation (Fig. 1), rapidly frozen, and freeze-dried to remove water without disrupting the lateral organization within the membrane [fig. S1 (*22*)]. Note that the lipid bilayers are fully hydrated prior to being frozen. Prior to NanoSIMS analysis, the geometries of the gel phase domains, which are thicker than the fluid phase regions, were characterized by AFM for subsequent comparison to the NanoSIMS data. As shown in Fig. 2D, the AFM image of the freeze-dried supported lipid bilayer contained domains that extended ~2.0 nm above the neighboring bilayer, in good agreement with the reported height difference (1.8 nm) between gel phase DSPC and fluid phase DLPC in a hydrated supported lipid bilayer on mica (*24, 25*).

For chemical imaging, the $^{13}C^{1}H^{-}$ and $^{12}C^{15}N^{-}$ NanoSIMS secondary ion signals were used to evaluate the distributions of $^{13}C_{18}$-DSPC and ^{15}N-DLPC, respectively, within the supported lipid bilayer. Although other secondary ions with a nominal mass of 14 ($^{12}C^{1}H_2^{-}$) and 27 amu ($^{13}C^{14}N^{-}$) were generated during analysis, the mass resolving power was sufficient to resolve the $^{13}C^{1}H^{-}$ and $^{12}C^{15}N^{-}$ ions from these interfering isobars while maintaining high lateral resolution, which permitted unambiguous identification of the species of interest. The component-specific NanoSIMS secondary ion images in Fig. 2A to C show that the bilayer was not homogeneous. Distinct microdomains enriched in $^{13}C_{18}$-DSPC, as evidenced by an increased $^{13}C^{1}H^{-}$ signal and decreased $^{12}C^{15}N^{-}$ signal, were dispersed within a ^{15}N-DLPC rich matrix. The area occupied by $^{13}C_{18}$-DSPC within the bilayer was lower than that based on the mol ratio of the lipids in the vesicle solution as prepared. This difference in the lipid composition between the vesicle solution and the phase separated supported lipid bilayer is likely due to selective adsorption of these very different lipid species (*26*).

Close examination of the sizes and shapes of the $^{13}C_{18}$-DSPC enriched domains observed in the NanoSIMS secondary ion images revealed that they were nearly identical to the domain geometry imaged by AFM at the same sample locations (Fig. 2D). Phase-separated domains with complex edge structures and domains as small as ~100 nm in diameter, as measured by AFM, are visible in the NanoSIMS secondary ion images (Fig. 2, circles), confirming the high lateral resolution and sensitivity of the NanoSIMS technique. A few of the features in the AFM image did not produce lipid-specific secondary ion signals (Fig. 2, arrows); the height difference between these features and the bilayer (> 5 nm, measured by AFM) confirmed that these objects were unlabeled debris and not lipid domains.

Quantitative information on the lipid composition within specified regions of the bilayer was obtained by calibrating the secondary ion yields using standard samples (*22*). Briefly, NanoSIMS measurements were made on sets of homogeneous supported lipid bilayers that systematically varied in the $^{13}C_{18}$-DSPC or ^{15}N-DLPC content, and calibration curves were constructed that correlated the normalized $^{13}C^{1}H^{-}$ or $^{12}C^{15}N^{-}$ signal intensities ($^{13}C^{1}H^{-}/^{12}C^{-}$ or $^{12}C^{15}N^{-}/^{12}C^{-}$) to the mol% of $^{13}C_{18}$-DSPC or ^{15}N-DLPC, respectively, within each sample [fig. S3 (*22*)]. With this approach, the gel phase lipid composition and uniformity were investigated by converting the component-specific secondary ion intensities collected at numerous locations within a single micrometer-sized domain into mol% concentrations (Fig. 3).

We could often detect compositional heterogeneity within the gel phase. Although the majority of the domain consisted of a ~9:1 mol ratio of $^{13}C_{18}$-DSPC to ^{15}N-DLPC, as predicted by the phase diagrams for DSPC and DLPC mixtures (*27-29*), higher concentrations of ^{15}N-DLPC were occasionally detected within the gel phase. To determine whether the ^{15}N-DLPC distribution within the gel phase domains varied in a statistically significant manner, each domain was divided into 3 by 3 pixel regions that did not include the domain edges or debris (Fig. 4), and the amount of ^{15}N-DLPC within each region was determined using the calibration curves. The variations in the ^{15}N-DLPC content within domains B and C (Fig. 4) were greater than the uncertainty in the measurements, indicating these domains contained statistically significant differences in lipid composition. AFM imaging revealed that the elevated ^{15}N-DLPC concentration localized within one $^{13}C_{18}$-DSPC enriched domain (Figs. 3 and 4, domain C) corresponded to a small (< 200 nm in diameter) fluid phase sub-domain within the gel phase (Fig. 3, circle). We hypothesize that small gel phase domains (tens of nanometers in diameter) that form early in the phase separation process coalesced around a small amount of ^{15}N-DLPC, thereby trapping the fluid phase sub-domain within the growing gel phase domain [see (*30*) for a theoretical model that may be relevant to this process]. A similar process may have produced the elevated concentrations of ^{15}N-DLPC that were detected at localized regions within other gel phase domains; however, the absence of topographical features that are characteristic of gel/fluid interfaces at these regions implies either that the fluid phase sub-domains were smaller than the lateral resolution of these AFM images, or the ^{15}N-DLPC was well dispersed within these small regions of the gel phase [note, the lateral resolution, ~70 nm, of these AFM images is significantly lower than the highest resolution attainable with AFM because relatively large areas (35 μm by 35 μm) were imaged at 512 by 512 pixels in order to locate regions for NanoSIMS analysis]. Lower concentrations of both lipids were measured in regions where debris is visible in the AFM images, and indicated that the non-lipid particles were embedded in the bilayer and could have served as nucleation sites. In the fluid phase, the lipid composition was again well approximated by phase diagrams (*27, 29*): the ratio of ^{15}N-DLPC to ^{13}C$_{18}$-DSPC was greater than 19:1 although tiny gel phase domains scattered throughout the fluid phase may have been included in this value.

Using component-specific secondary ion imaging performed with the NanoSIMS, domains as small as ~100 nm in diameter were successfully imaged within a phase-separated lipid membrane, the lipid composition within small regions of the bilayer were quantified, and heterogeneous lipid distributions within gel phase domains were identified. This example of phase-separated membrane domains also demonstrates the advantage of combining quantitative lipid composition analysis performed by the NanoSIMS with multiple imaging modalities. Because supported lipid bilayers are amenable to isotopic substitution and freeze-drying, this approach can establish the distributions of multiple lipids and membrane-anchored proteins within more complex phase-separated supported membranes by incorporating a distinct stable isotope into each membrane component of interest and simultaneously imaging the secondary ions that distinguish each species. To extend this approach to living cells, stable isotopes can be selectively incorporated into membrane components by modifying techniques to radiolabel lipid components in live cells (*31, 32*), and cell membranes can be isolated with methods to detach intact membrane sheets from live cells (*33-36*). In this way, quantitative information on multiple components within native cell membranes may be obtained with high lateral resolution.

References

1. K. Simons, D. Toomre, *Nat. Rev. Mol. Cell Biol.* **1**, 31 (2000).
2. D. A. Brown, E. London, *Annu. Rev. Cell Dev. Biol.* **14**, 111 (1998).
3. M. Edidin, *Ann. Rev. Biophys. Biomol. Struct*. **32**, 257 (2003).
4. G. W. Feigenson, J. T. Bulboltz, *Biophys. J.* **80**, 2775 (2001).
5. B. Stottrup, D. S. Stevens, S. L. Keller, *Biophys. J.* **88**, 269 (2005).
6. A. K. Kenworthy, N. Petranova, M. Edidin, *Mol. Biol. Cell* **11**, 1645 (2000).
7. J. Korlach, P. Schwille, W. W. Webb, G. W. G. W. Feigenson, *Proc. Natl. Acad. Sci. U.S.A.* **96**, 8461 (1999).
8. N. Kahya, D. Scherfeld, K. Bacia, P. Schwille, *J. Struct. Biol.* **147**, 77 (2004).
9. J. E. Shaw et al., *Biophys. J.* **90**, 2170 (2006).
10. D. C. Fernandez, R. Bhargava, S. M. Hewitt, I. W. Levin, *Nat. Biotechnol.* **23**, 469 (2005).
11. E. O. Potma, X. S. Xie, *ChemPhysChem* **6**, 77 (2005).
12. A. R. Burns, *Langmuir* **19**, 8358 (2003).
13. J. C. Lawrence, D. E. Saslowsky, J. M. Edwardson, R. M. Henderson, *Biophys. J.* **84**, 1827 (2003).
14. C. Yuan, J. Furlong, P. Burgos, L. J. Johnston, *Biophys. J.* **82**, 2526 (2002).
15. N. Bourdos et al., *Biophys. J.* **79**, 357 (2000).
16. A. G. Sostarecz, C. M. McQuaw, A. G. Ewing, N. Winograd, *J. Am. Chem. Soc.* **126**, 13882 (2004).
17. M. L. Pachloski, D. M. Cannon, A. G. Ewing, N. Winograd, *J. Am. Chem. Soc.* **121**, 4716 (1999).
18. J.-L. Guerquin-Kern, T.-D. Wu, C. Quintana, A. Croisy, *Biochim. Biophys. Acta* **1724**, 228 (2005).
19. C. Galli Marxer, M. L. Kraft, P. K. Weber, I. D. Hutcheon, S. G. Boxer, *Biophys. J.* **88**, 2965 (2005).
20. R. Peteranderl, C. Lechene, *J. Am. Soc. Mass Spectrom.* **15**, 478–485 (2004).
21. S. G. Ostrowski, C. T. Van Bell, N. Winograd, A. G. Ewing, *Science* **305**, 71 (2004).
22. Supporting information and data available at Science Online.
23. J. T. Groves, N. Ulman, S. G. Boxer, *Science* **275**, 651 (1997).
24. T. V. Ratto, M. L. Longo, *Biophys. J.* **83**, 3380 (2002).
25. W. C. Lin, C. Blanchette, T. V. Ratto, M. L. Longo, *Biophys. J.* **90**, 228 (2006).
26. C. Blanchette, W. C. Lin, T. V. Ratto, M. L. Longo, *Biophys. J.* **90**, 4466 (2006).
27. S. Mabrey, J. M. Sturtevant, *Proc. Natl. Acad. Sci. U.S.A.* **73**, 3862 (1976).
28. R. E. Jacobs, B. S. Hudson, H. C. Andersen, *Biochemistry* **16**, 4349 (1977).
29. J. H. Ipsen, O. G. Mouritsen, *Biochim. Biophys. Acta* **944**, 121 (1988).
30. V. A. J. Frolov, Y. A. Chizmadzhev, F. S. Cohen, J. Zimmerberg, *Biophys. J.* **91**, 189 (2006).
31. G. van Echten, R. Birk, G. Brenner-Weiss, R. R. Schmidt, K. Sandhoff, *J. Biol. Chem.* **265**, 9333 (1990).
32. P. Keller, K. Simons, *J. Cell Bio.* **140**, 1357 (1998).
33. S. T. Hess et al., *J. Cell Bio*. **169**, 965 (2005).

34. J. B. Perez, K. L. Martinez, J. M. Segura, H. Vogel, *Adv. Funct. Mater.* **16**, 306 (2006).
35. F. Drees, A. Reilein, W. J. Nelson, *Methods Mol. Biol.* **294**, 303 (2004).
36. S. Yamada, S. Pokutta, F. Drees, W. I. Weis, W. J. Nelson, *Cell* 123, 889 (2005).
37. We thank W. C. Lin and C. Blanchette for their help in forming phase-separated-samples, and L. R. Nittler (Carnegie Institution of Washington) for the development of the image processing software. M.L.K is supported by an NIH NRSA fellowship. This work is supported by grants from the NSF Biophysics program and NIH GM06930 (to S.G.B.), and the work at LLNL was performed under the auspices of the U.S. Department of Energy by the University of California, Lawrence Livermore National Laboratory under Contract W-7405-Eng-48 and Contract DE-AC52-07NA27344. We are grateful to the Stanford Nanofabrication Facility for fabrication and the NSF MRSEC CPIMA for analysis (ellipsometry and AFM).

1. K. Simons, D. Toomre, *Nat. Rev. Mol. Cell Biol.* **1**, 31 (2000).
2. D. A. Brown, E. London, *Ann. Rev. Cell Dev. Biol.* **14**, 111 (1998).
3. M. Edidin, *Ann. Rev. Biophys. Biomol. Struct.* **32**, 257 (2003).
4. G. W. Feigenson, J. T. Bulboltz, *Biophys. J.* **80**, 2775 (2001).
5. B. Stottrup, D. S. Stevens, S. L. Keller, *Biophys. J.* **88**, 269 (2005).
6. A. K. Kenworthy, N. Petranova, M. Edidin, *Mol. Biol. Cell* **11**, 1645 (2000).
7. J. Korlach, P. Schwille, W. W. Webb, G. W. G. W. Feigenson, *Proc. Natl. Acad. Sci. U.S.A.* **96**, 8461 (1999).
8. N. Kahya, D. Scherfeld, K. Bacia, P. Schwille, *J. Struct. Biol.* **147**, 77 (2004).
9. J. E. Shaw *et al.*, *Biophys. J.* **90**, 2170 (2006).
10. D. C. Fernandez, R. Bhargava, S. M. Hewitt, I. W. Levin, *Nat. Biotechnol.* **23**, 469 (2005).
11. E. O. Potma, X. S. Xie, *ChemPhysChem* **6**, 77 (2005).
12. A. R. Burns, *Langmuir* **19**, 8358 (2003).
13. J. C. Lawrence, D. E. Saslowsky, J. M. Edwardson, R. M. Henderson, *Biophys. J.* **84**, 1827 (2003).
14. C. Yuan, J. Furlong, P. Burgos, L. J. Johnston, *Biophys. J.* **82**, 2526 (2002).
15. N. Bourdos *et al.*, *Biophys. J.* **79**, 357 (2000).
16. A. G. Sostarecz, C. M. McQuaw, A. G. Ewing, N. Winograd, *J. Am. Chem. Soc.* **126**, 13882 (2004).
17. M. L. Pachloski, D. M. Cannon, A. G. Ewing, N. Winograd, *J. Am. Chem. Soc.* **121**, 4716 (1999).
18. J.-L. Guerquin-Kern, T.-D. Wu, C. Quintana, A. Croisy, *Biochim. Biophys. Acta* **1724**, 228 (2005).
19. C. Galli Marxer, M. L. Kraft, P. K. Weber, I. D. Hutcheon, S. G. Boxer, *Biophys. J.* **88**, 2965 (2005).
20. R. Peteranderl, C. Lechene, *J. Am. Soc. Mass Spectrom.* **15**, 478–485 (2004).
21. S. G. Ostrowski, C. T. Van Bell, N. Winograd, A. G. Ewing, *Science* **305**, 71 (2004).
22. Supporting information and data available at Science Online.
23. J. T. Groves, N. Ulman, S. G. Boxer, *Science* **275**, 651 (1997).
24. T. V. Ratto, M. L. Longo, *Biophys. J.* **83**, 3380 (2002).

25. W. C. Lin, C. Blanchette, T. V. Ratto, M. L. Longo, *Biophys. J.* **90**, 228 (2006).
26. C. Blanchette, W. C. Lin, T. V. Ratto, M. L. Longo, *Biophys. J.* **90**, 4466 (2006).
27. S. Mabrey, J. M. Sturtevant, *Proc. Natl. Acad. Sci. U.S.A.* **73**, 3862 (1976).
28. R. E. Jacobs, B. S. Hudson, H. C. Andersen, *Biochemistry* **16**, 4349 (1977).
29. J. H. Ipsen, O. G. Mouritsen, *Biochim. Biophys. Acta* **944**, 121 (1988).
30. V. A. J. Frolov, Y. A. Chizmadzhev, F. S. Cohen, J. Zimmerberg, *Biophys. J.* **91**, 189 (2006).
31. G. van Echten, R. Birk, G. Brenner-Weiss, R. R. Schmidt, K. Sandhoff, *J. Biol. Chem.* **265**, 9333 (1990).
32. P. Keller, K. Simons, *J. Cell Bio.* **140**, 1357 (1998).
33. S. T. Hess *et al.*, *J. Cell Bio.* **169**, 965 (2005).
34. J. B. Perez, K. L. Martinez, J. M. Segura, H. Vogel, *Adv. Funct. Mater.* **16**, 306 (2006).
35. F. Drees, A. Reilein, W. J. Nelson, *Methods Mol. Biol.* **294**, 303 (2004).
36. S. Yamada, S. Pokutta, F. Drees, W. I. Weis, W. J. Nelson, *Cell* **123**, 889 (2005).

37. We thank W. C. Lin and C. Blanchette for their help in forming phase-separated-samples, and L. R. Nittler (Carnegie Institution of Washington) for the development of the image processing software. M.L.K is supported by an NIH NRSA fellowship. This work is supported by grants from the NSF Biophysics program and NIH GM06930 (to S.G.B.), and the work at LLNL was performed under the auspices of the U.S. Department of Energy by the University of California, Lawrence Livermore National Laboratory under Contract W-7405-Eng-4. We are grateful to the Stanford Nanofabrication Facility for fabrication and the NSF MRSEC CPIMA for analysis (ellipsometry and AFM).

Supporting Online Material
Materials and Methods
Figs. S1 to S4
Tables S1 to S4
References

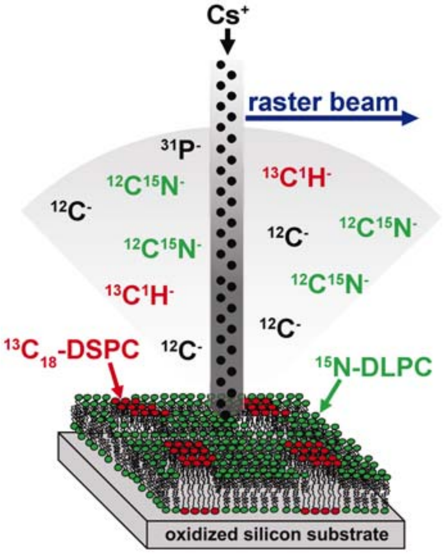
Cs+
raster beam
31P-
12C15N-
13C1H-
12C-
12C-
12C15N-
12C15N-
12C15N-
12C15N-
13C1H-
12C-
13C18-DSPC
12C-
15N-DLPC
oxidized silicon substrate

Fig. 1. Schematic shows NanoSIMS analysis of phase-separated lipid bilayer (not to scale). At room temperature, gel and fluid phases are present in the bilayer, which are mostly composed of $^{13}C_{18}$-DSPC (red) and ^{15}N-DLPC (green), respectively. The gel phase is ~2 nm higher than the neighboring fluid phase and can be imaged by AFM (compare with Fig. 2D). The sample is freeze-dried to preserve the lateral organization within the bilayer [fig. S1 (*22*)], and analyzed with the NanoSIMS. During NanoSIMS analysis, a focused $^{133}Cs^+$ ion beam generates secondary ions; the negative ions are collected and analyzed in a high-resolution mass spectrometer. The secondary ions that are characteristic of $^{13}C_{18}$-DSPC and ^{15}N-DLPC, $^{13}C^{1}H^-$ and $^{12}C^{15}N^-$, respectively, are used to identify each component in the NanoSIMS image. The $^{133}Cs^+$ primary ion beam is focused to a ~100 nm-diameter spot [fig. S2 (*22*)] and is rastered across the sample to generate an image.

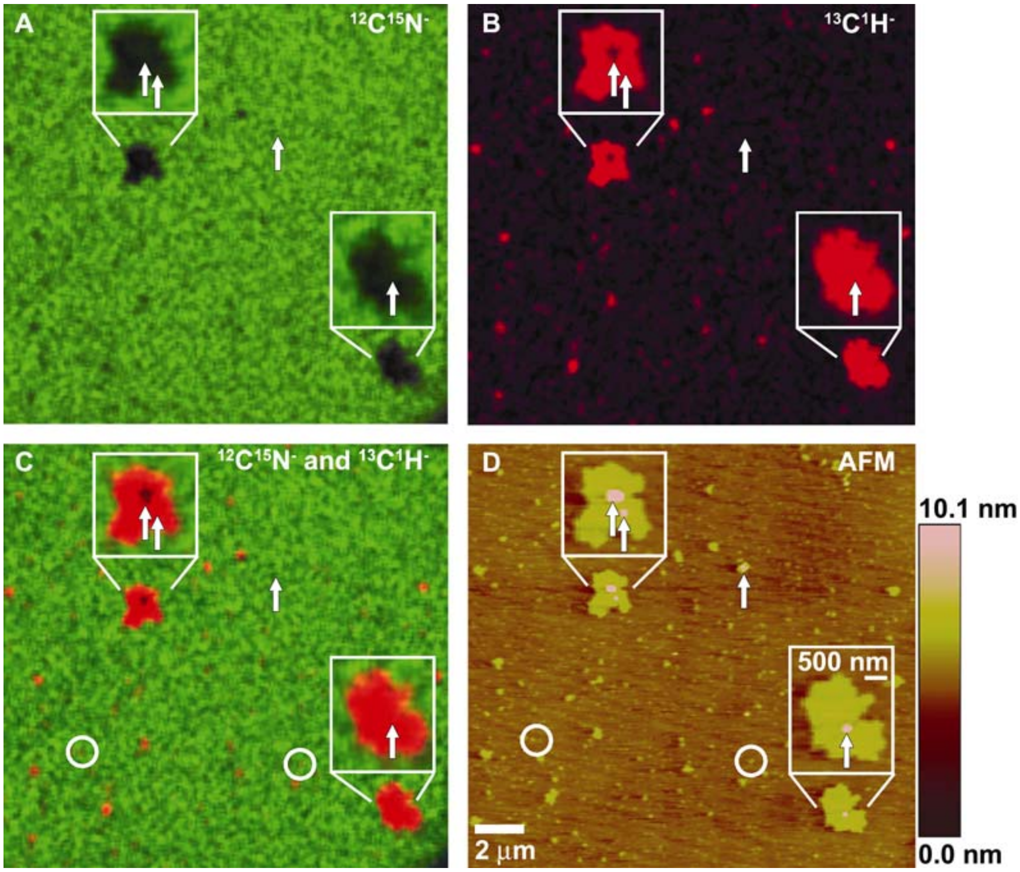

Fig. 2. A phase-separated supported lipid bilayer that was freeze-dried and imaged by NanoSIMS and AFM. (**A**–**C**) NanoSIMS images of the normalized $^{12}C^{15}N^-$ signal that localizes ^{15}N-DLPC, the $^{13}C^1H^-$ signal that localizes $^{13}C_{18}$-DSPC, and the overlaid $^{12}C^{15}N^-$ and $^{13}C^1H^-$ signals, respectively; (**D**) an AFM image of the same region on the sample taken prior to NanoSIMS analysis. The contrast levels within the NanoSIMS images reflect the normalized signal intensity, corresponding to 100 and 0 mol% of the appropriate isotopically labeled lipid, as determined from calibration curves [see text and supporting information (*22*)]. Arrows indicate objects in the AFM images that are unlabeled debris, not domains, and their corresponding locations in the NanoSIMS images. Domains with diameters as small as ~100 nm, as measured by AFM, were visible in the SIMS images (e.g., those highlighted with circles). NanoSIMS images were acquired with a pixel size of ~100 nm by 100 nm.

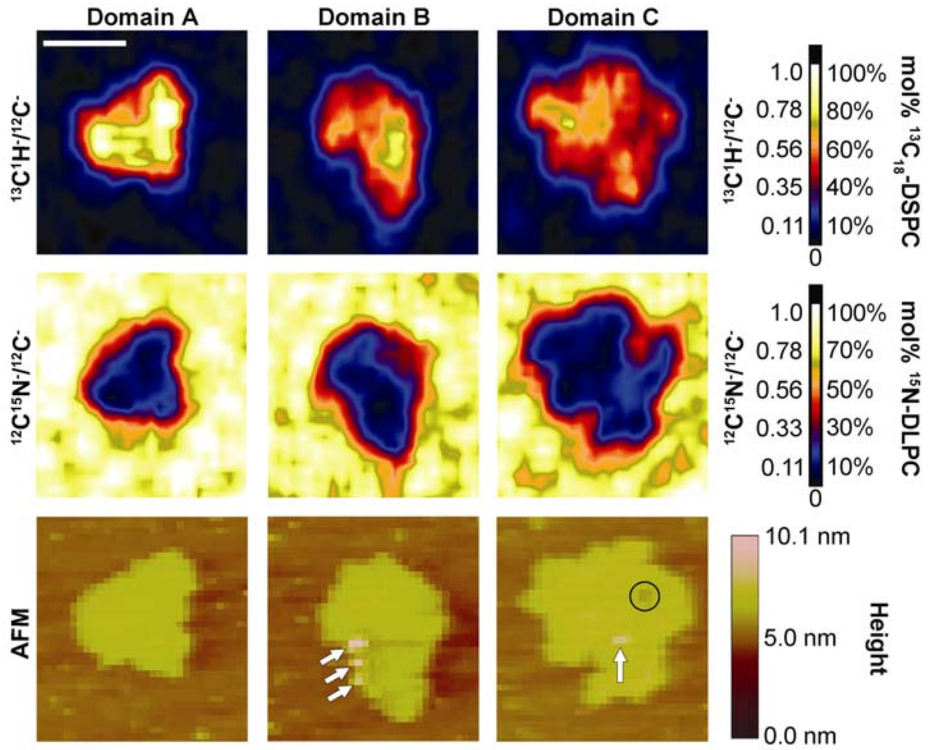

Fig. 3. Details of correlated NanoSIMS and AFM images showing domain composition and topography. The $^{13}C^{1}H^{-}/^{12}C^{-}$ and $^{12}C^{15}N^{-}/^{12}C^{-}$ NanoSIMS isotope ratio images show the abundance of $^{13}C_{18}$-DSPC and ^{15}N-DLPC, respectively, within the bilayer, as determined from calibration curves [fig. S3 (*22*)]. AFM images acquired at the same sample locations reveal topography. Lower concentrations of both lipids were detected in the locations where debris was identified (arrows). The lipid composition within the gel phase was usually consistent with the phase diagram predictions (domain A), but elevations in the amount of ^{15}N-DLPC within the gel phase were occasionally detected at localized areas within the domains (domains B and C). AFM imaging indicated a small (< 200 nm) depression that could be a fluid phase sub-domain (circle) trapped within the gel phase (domain C); this is confirmed by the NanoSIMS image, which shows an elevated amount of ^{15}N-DLPC across this region (see also Fig. 4). NanoSIMS images were acquired with a pixel size of 100 nm by 100 nm and are smoothed over three pixels. Scale bar is 1 μm.

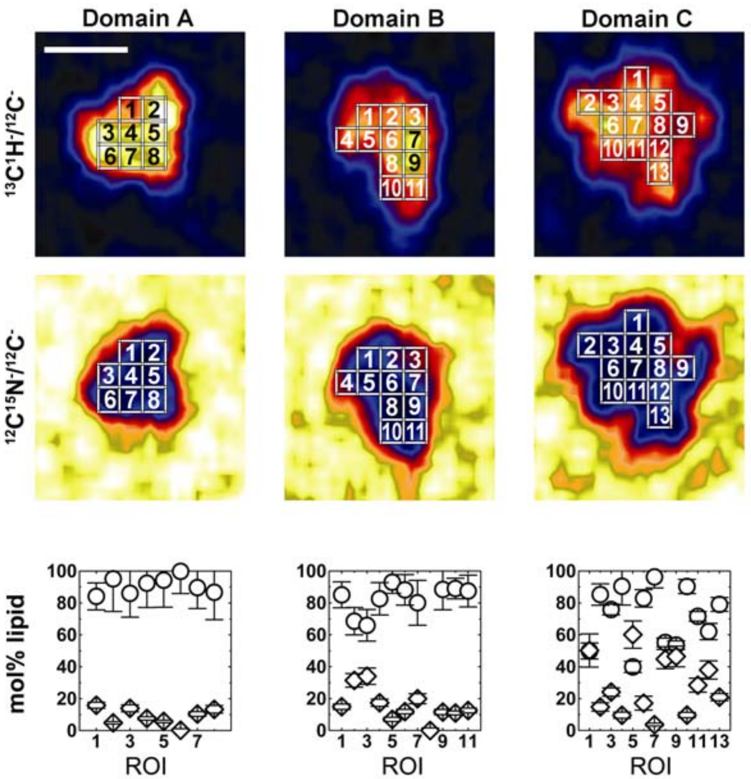

Fig. 4. Quantitative analysis of the gel phase domains shown in Fig. 3. Each gel phase domain was divided into 3 by 3 pixel regions; specific regions of interest (ROIs) within each domain are shown on the NanoSIMS images. The graphs illustrate the amount of $^{13}C_{18}$-DSPC (○) and ^{15}N-DLPC (◇) detected within each domain for the numbered ROI, where each data point represents a 3 by 3 pixel region within a domain, and the error bars represent the uncertainty calculated using counting statistics [supporting online text, fig. S4 (*22*)]. Statistically significant lateral variations in lipid composition were detected in domain C, where ROIs 5, 8, and 9 are in the vicinity of the fluid phase sub-domain that was detected by AFM (Fig. 3, domain C, circled region). NanoSIMS images were acquired with a pixel size of 100 nm by 100 nm and are smoothed over three pixels. Scale bar is 1 μm.